NANO LETTERS

Letter

pubs.acs.org/NanoLett

Nonequilibrium-Plasma-Synthesized ZnO Nanocrystals with Plasmon Resonance Tunable via Al Doping and Quantum Confinement

Benjamin L. Greenberg,[†] Shreyashi Ganguly,[†,‡] Jacob T. Held,[‡] Nicolaas J. Kramer,[†] K. Andre Mkhoyan,[‡] Eray S. Aydil,[‡] and Uwe R. Kortshagen*[,†]

[†]Department of Mechanical Engineering and [‡]Department of Chemical Engineering and Materials Science, University of Minnesota, Minneapolis, Minnesota 55455, United States

Supporting Information

ABSTRACT: Metal oxide semiconductor nanocrystals (NCs) exhibit localized surface plasmon resonances (LSPRs) tunable within the infrared (IR) region of the electromagnetic spectrum by vacancy or impurity doping. Although a variety of these NCs have been produced using colloidal synthesis methods, incorporation and activation of dopants in the liquid phase has often been challenging. Herein, using Al-doped ZnO (AZO) NCs as an example, we demonstrate the potential of nonthermal plasma synthesis as an alternative strategy for the production of doped metal oxide NCs. Exploiting unique, thoroughly nonequilibrium synthesis conditions, we obtain NCs in which dopants are not segregated to the NC surfaces and local doping levels are high near the NC centers. Thus, we achieve overall doping levels as high as 2×10^{20} cm^{-3} in NCs with diameters ranging from 12.6 to 3.6 nm, and for the first time experimentally demonstrate a clear quantum confinement blue shift of the LSPR energy in vacancy- and impurity-doped semiconductor NCs. We propose that doping of central cores and heavy doping of small NCs are achievable via nonthermal plasma synthesis, because chemical potential differences between dopant and host atoms—which hinder dopant incorporation in colloidal synthesis—are irrelevant when NC nucleation and growth proceed via irreversible interactions among highly reactive gas-phase ions and radicals and ligand-free NC surfaces. We explore how the distinctive nucleation and growth kinetics occurring in the plasma influences dopant distribution and activation, defect structure, and impurity phase formation.

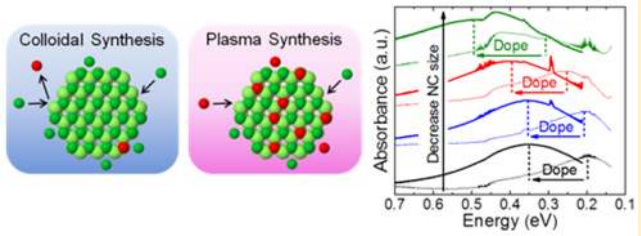

KEYWORDS: *plasma, nanocrystals, doping, plasmonics, quantum confinement, aluminum-doped zinc oxide*

In the past half decade, the colloidal synthesis community has developed an extensive library of doped metal oxide semiconductor nanocrystals (NCs) exhibiting tunable infrared (IR) localized surface plasmon resonances (LSPRs), including vacancy-doped tungsten oxide[1] and aliovalently doped oxides of indium,[2−4] cadmium,[5] titanium,[6] and zinc.[7−9] Near-IR applications include electrochromic sunlight management[10] and solar energy harvesting,[11] and mid-IR applications include IR light-emitting diode efficiency enhancement[12] and surface-enhanced IR absorption spectroscopy.[13] Varying the dopant or vacancy concentrations in these materials modulates the free carrier concentration and, thus, the LSPR energy. Recently, a blue shift in LSPR energy has also been achieved via quantum confinement in sufficiently small photodoped ZnO NCs.[14]

Throughout the development of these materials, synthetic challenges have included finding molecules suitable for electronic passivation of surface defects, attaining high dopant activation fractions (fraction of dopant atoms serving as charge carrier donors), achieving uniform radial distributions of dopants within an NC, and simultaneously controlling doping level and NC size. Although substantial progress has been made in addressing these challenges in the liquid phase,[3,15−18] it has been difficult to simultaneously fulfill all of these requirements for diverse materials using a single synthesis technique. Nonthermal plasma synthesis is emerging as an alternative method for synthesizing materials inherently inaccessible by liquid phase routes, such as plasmonic P-doped Si.[19] However, until now the plasma synthesis approach has not been used for producing materials that are also accessible by colloidal synthesis, such as impurity-doped compound semiconductor NCs; exploring materials accessible by both colloidal and plasma synthesis allows assessment of the fundamental differences in dopant incorporation and activation mechanisms between these two methods. The nonthermal plasma approach is attractive not only as a novel chemical route, but also as a scalable, high-throughput, low-temperature process that, when integrated with inertial impaction deposition, is capable of producing high-performance nanocrystalline thin films suitable for myriad optoelectronic applications.[20]

Here, we report nonthermal plasma synthesis of ligand-free, heavily Al-doped ZnO (AZO) NCs with high dopant activation fractions. Importantly, high doping levels are attained even within the cores of the NCs, a feat that has been difficult to achieve because dopants tend to segregate toward NC surfaces

Received: September 7, 2015
Revised: November 2, 2015
Published: November 9, 2015

DOI: 10.1021/acs.nanolett.5b03600
Nano Lett. 2015, 15, 8162−8169

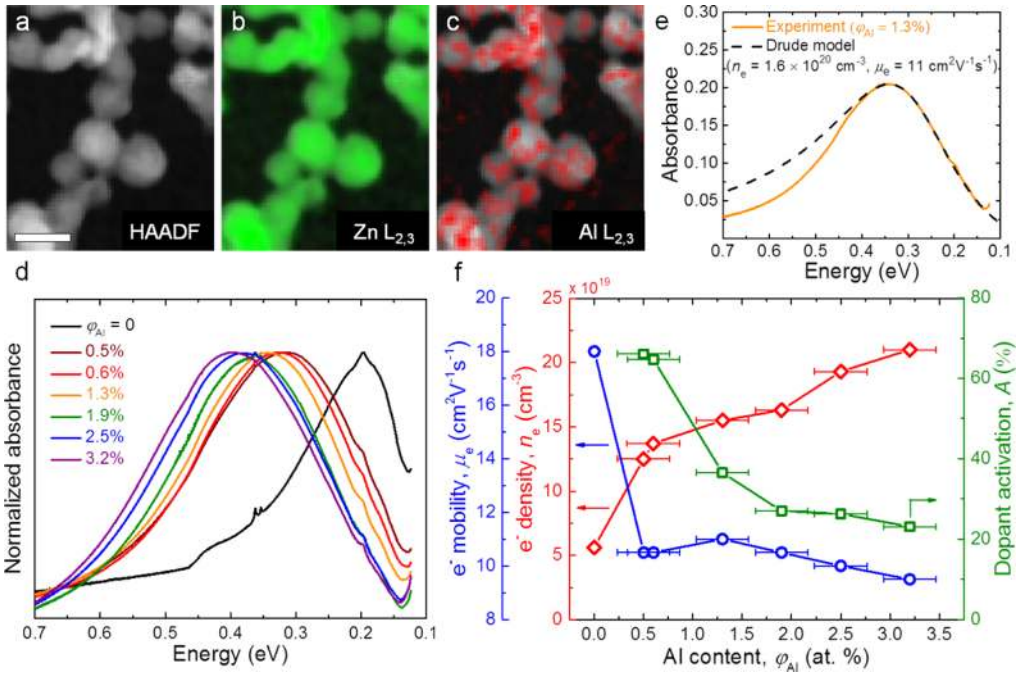

Figure 1. (a) HAADF-STEM image of AZO NCs with φ_{Al} = 1.3%. The scale bar is 10 nm (b–c) Spectrum images of Zn and Al $L_{2,3}$ edges overlaid on the HAADF-STEM image. HAADF-STEM and EELS maps are acquired simultaneously. (d) FTIR absorption spectra of NCs with φ_{Al} ranging from 0 to 3.2% and diameters between ~7 and 9.5 nm. (NC diameter gradually decreases from 9.5 to ~7 nm with increasing φ_{Al}). In this size range, both the broadening and the blue shift of the LSPR peak with increasing φ_{Al} are due primarily to Al doping—the former to decreased μ_e (ionized impurity scattering) and the latter to increased n_e. The strong dependence of line width (μ_e) on φ_{Al} is characteristic of high local doping levels in the NC cores. (e) Representative fit (dashed black line) of an LSPR absorption feature (solid orange line) using the Drude model and Mie theory. The discrepancy between model and experiment on the high-energy side is also consistent with high local doping levels in the NC cores. (f) Electron densities, n_e (red diamonds), and electron mobilities, μ_e (blue circles), extracted from fits, and dopant activation fractions, A (green squares), calculated using eq 1.

during colloidal synthesis. Doping of the cores is evinced by the high activation fractions, the line shapes of the LSPR absorption features, and elemental maps produced by electron energy loss spectroscopy performed in a scanning transmission electron microscope (STEM-EELS). Moreover, we demonstrate that high *spatially averaged* doping levels (i.e., overall doping levels observable in ensemble measurements) can be maintained as NC size is reduced from 11.3 to 3.6 nm, which suggests high *local* doping levels not only beneath the outermost surface layers but deep within the cores, near the NC centers. Such dopant distributions enable simultaneous control of doping level and NC size, which we use to clearly experimentally demonstrate, for the first time, a quantum confinement effect on the LSPR energy of impurity-doped semiconductor NCs.

In a typical synthesis, diethylzinc (DEZ) and trimethylaluminum (TMA) are injected into a low-pressure (5.6 Torr) radio frequency Ar/O_2 plasma to form an aerosol containing AZO NCs. The aerosol accelerates through a rectangular slit orifice and the NCs, attaining supersonic velocities, deposit via inertial impaction onto a variety of substrates, forming nanocrystalline thin films at a deposition rate of 10 to 20 nm/s. Typical films are 500 ± 50 nm thick with 65 ± 5% porosity (ZnO volume fraction of ~35%). As deposited, the films have low free electron densities (n_e) due to hydroxyl groups on the NC surfaces acting as electron traps; we eliminate these traps by using atomic layer deposition (ALD) to infill the films with Al_2O_3, forming a ZnO/Al_2O_3 composite with a porosity of 10 ± 5%. A previous study of oxygen-vacancy-doped ZnO NCs[21] demonstrated that the ALD infill removes surface OH groups and seals the NCs, resulting in air-stable conductive films with n_e sufficient to support LSPR at ~0.2 eV.

We control the Al doping level and thus the LSPR energy by varying the TMA concentration in the precursor feed gas. Increasing the TMA feed rate results in a linearly proportional rise of the Al concentration in the films ([Al]/[Zn+Al] atomic fraction, hereafter referred to as φ_{Al}) measured by inductively coupled plasma mass spectroscopy (Figure S1 in the Supporting Information). STEM-EELS spectrum images (Figure 1a–c) indicate that Al atoms reside throughout the NCs including the NC cores and that Al is not segregated to the NC surfaces; the apparent clusters of Al atoms that do reside on NC surfaces will be discussed later. As shown in Figure 1d, incrementing φ_{Al} from 0 to 3.2% results in an LSPR blue shift from ~0.2 to ~0.4 eV, indicating increasing incorporation of Al into the ZnO lattice and donation of its surplus valence electron to the conduction band.[7] The broadening of the LSPR feature indicates increased electron scattering,[22] which is also consistent with Al incorporation.[3] Further evidence for electronically active Al is provided by UV–vis spectra which reveal optical bandgaps (E_g) blue-shifted due to the Burstein–Moss effect[23] (see Figure S5 in the Supporting Information). We note that the increase in φ_{Al} is also accompanied by an incidental NC size reduction from 9.5 to ~7 nm (see Figure S4 in the Supporting Information), which, as discussed later, partially contributes to the LSPR blue shift, though minimally (<0.01 eV) in this size range.

Theoretical fits of the LSPR features in Figure 1d indicate high local doping levels in the NC cores, beneath the NC

DOI: 10.1021/acs.nanolett.5b03600
Nano Lett. 2015, 15, 8162–8169

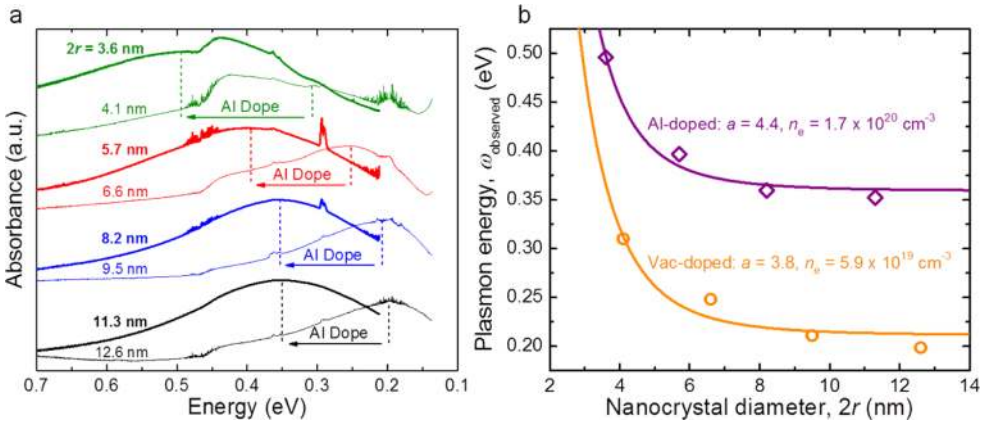

Figure 2. (a) FTIR spectra of vacancy-doped NCs (φ_{Al} = 0) with diameters ranging from 12.6 to 4.1 nm (thin lines) and Al-doped NCs (φ_{Al} = 1.3%) with diameters ranging from 11.3 to 3.6 nm (thick lines). Spectra are paired by slit orifice size used during synthesis (e.g., the black spectra correspond to the largest NCs, which were produced with the thinnest orifice), and for a given orifice size, Al-doped NCs are slightly smaller (e.g., 11.3 vs 12.6 nm) due to the incidental effect of Al doping on NC size. Comparing spectra of different colors, the blue shifts and broadenings of the LSPRs with decreasing NC size are due to quantum confinement. In comparing spectra of the same color, this size effect alone cannot account for the blue shifts, that is, Al doping increases n_e. The absorption feature emerging around 0.44 eV indicates the presence of OH groups on the film surfaces. This vibrational feature becomes more pronounced as LSPR absorption diminishes and broadens with decreasing NC size. (b) LSPR energy vs NC diameter for φ_{Al} = 0 (orange circles) and φ_{Al} = 1.3% (purple diamonds) with fits from eq 2.

surface layers. To produce these fits we use Mie theory with the classical Drude dielectric function, assuming frequency-independent damping (for details, see ref 16) and thus obtain estimates of the free electron densities (n_e) and intraparticle mobilities (μ_e). A representative comparison of this model and experimental data is shown in Figure 1e. For all φ_{Al}, such comparisons show good agreement at low energy but substantially underestimate the line width on the high-energy side. According to a recent study of tin-doped indium oxide (ITO) NCs,[3] this divergence at high energy indicates that damping is dominated by frequency-dependent ionized impurity scattering (in agreement with the LSPR peak broadening), which in turn suggests that dopants are abundant in the NC cores as opposed to segregated to the surfaces, where they would not contribute strongly to damping. However, neglecting this frequency dependence introduces only a small error (~10%) to our estimates of n_e,[3] which coincidentally cancels with that associated with neglecting particle−particle interactions.[24,25]

Additional evidence of high local doping levels in the NC cores is provided by the dopant activation fractions (A), that is, the numbers of additional free electrons per Al atom in the samples, which we calculate assuming constant oxygen vacancy concentration

$$A(\varphi_{Al}) = \frac{n_e(\varphi_{Al}) - n_e(\varphi_{Al} = 0)}{n_{Al}(\varphi_{Al})} \quad (1)$$

In solution-synthesized NCs, A is often low; for example, in solution-synthesized ITO NCs, A values of 9−17% have been reported.[24] Recently, careful selection of In and Sn precursors based on relative reactivities has led to A values as high as 71%.[3] However, recent work by the same group on AZO NCs with φ_{Al} = 1.8 and 2.5% has resulted in A values of 2 and 5%, respectively; this significant inefficiency was attributed to segregation of Al atoms to the NC surfaces, where compensation by electron acceptors is more likely than donation to the conduction band.[8] In contrast, the plasma-synthesized AZO NCs reported here exhibit A greater than 20% for all φ_{Al} between 0.5 and 3.2%, with a maximum A of 66% for φ_{Al} = 0.5% (Figure 1f).

To further modulate the LSPR energy, NC size can be used as an additional handle, provided that heavy doping is maintained as NC size is reduced. Using photodoping to maintain a constant n_e of 1.4 × 10^{20} cm^{-3}, Schimpf et al. showed that reducing NC diameter from 12 to 3.5 nm blue-shifted the LSPR energy from ~0.25 to ~0.5 eV, which they attributed to the coupling of collective plasmonic excitations to single-electron intraband transitions whose energies increase with quantum confinement.[14] A similar blue shift has been observed in metal (Ag) nanoparticles,[26−30] but to our knowledge, there are no reports of experimental demonstrations of this confinement effect in vacancy- or impurity-doped semiconductor NCs.

As mentioned previously, NC size is slightly reduced when φ_{Al} is increased. To explore a wider range of NC sizes and to resolve the effects of doping and size reduction on the LSPR energy, we introduce an independent handle on NC size: we vary the width of the rectangular slit orifice separating the synthesis and the deposition regions while maintaining constant precursor mass flow rates. Increasing the slit width reduces the gas pressure (from 14.5 to 0.9 Torr) as well as the residence time of the gas and the particles in the synthesis region (from ~50 to ~3 ms). These reductions in pressure and residence time decrease the total number of collisions between reactive species and NCs during synthesis and thus truncate NC growth. Using slit widths ranging from 0.5 to 3.5 mm, vacancy-doped (φ_{Al} = 0) NC size can be varied from 12.6 to 4.1 nm, and Al-doped (φ_{Al} = 1.3%) NC size can be varied from 11.3 to 3.6 nm (NC sizes determined from XRD peak width using the Scherrer formula, see Figure S2 in the Supporting Information). Film thickness and porosity, however, remain constant and, as usual, we use ALD to infill the films with Al_2O_3 in order to remove and seal out electron-trapping OH groups.

Figure 2a displays the IR spectra of vacancy-doped (φ_{Al} = 0, doped only by oxygen vacancies) and Al-doped (φ_{Al} = 1.3% and oxygen vacancies presumably still present) NCs produced using four orifice widths, which reveal the effect of quantum

DOI: 10.1021/acs.nanolett.5b03600
Nano Lett. 2015, 15, 8162−8169

confinement on the LSPR energy. For $\varphi_{Al} = 0$, as NC diameter is reduced from 12.6 to 4.1 nm, the LSPR energy blue shifts from 0.20 to 0.31 eV, and for $\varphi_{Al} = 1.3\%$, as NC diameter is reduced from 11.3 to 3.6 nm, the LSPR energy blue shifts from 0.35 to 0.50 eV; in both cases, the blue shift is accompanied by line broadening. Both the blue shifts as well as the broadenings are similar in magnitude to those observed by Schimpf et al. for similarly sized photodoped ZnO NCs.[14]

Fitting a plot of LSPR energy vs NC size (Figure 2b) confirms that the LSPR blue shifts are due to quantum confinement. Dependence of the LSPR energy on NC size can be described using a Lorentz oscillator model in which quantum confinement modifies both the driving and restoring forces.[14,30] For the purposes of this study, however, we favor an approach that has emerged from a recent density-functional-theory study that consolidates size dependences of the LSPR in an intuitive, albeit phenomenological, single formula. Specifically, Zhang et al.[31] used density functional theory to calculate the LSPR energies of 4 nm diameter CdSe NCs and 5 nm CuS and CuSe NCs with free carrier (hole) densities ranging from 0 to $\sim 10^{22}$ cm^{-3} and subsequently introduced a simple phenomenological formula for the LSPR energy of an NC of radius r

$$\omega_{observed}^{\ 2} = \omega_{classical}^{\ 2} + \left(\frac{a\hbar^2}{m_e^* r^2}\right)^2 \quad (2)$$

where $\omega_{observed}$ is the observed LSPR energy, $\omega_{classical}$ is the corresponding material-dependent classical LSPR energy (observed for $r \rightarrow \infty$), m_e^* is the electron effective mass (overall inertial mass of an oscillating electron), and a is a proportionality constant. Using eq 2 to fit the data in Figure 2b, we find a to be 3.8 and 4.4 for vacancy-doped and Al-doped ZnO NCs, respectively, in good agreement with the value used to fit the theoretical CdSe data ($a \approx 4$). Using the classical Drude model to convert $\omega_{classical}$ to n_e, we obtain n_e values of 5.9×10^{19} and 1.7×10^{20} cm^{-3} for vacancy-doped and Al-doped ZnO NCs, respectively, and the Burstein−Moss shifts apparent in the corresponding ultraviolet−visible (UV−vis) spectra (Figure S2 in the Supporting Information) confirm that n_e is in fact consistently higher in the Al-doped NCs. Although we cannot completely rule out the possibility that with decreasing NC size, n_e increases slightly and contributes to LSPR blue shifts, the good agreement of our data with Zhang's theoretical results as well as Schimpf's experimental results indicates that quantum confinement is the primary contributor.

These results are significant not only as an experimental demonstration of a quantum confinement effect on the LSPR energy of impurity-doped NCs but also as evidence of effective impurity doping over a wide range of NC sizes. In fact, we suspect that the lack of reports on this quantum confinement effect is due partially to difficulty, in colloidal synthesis, of attaining high doping levels in very small NCs. To our knowledge, the smallest previously reported AZO NCs exhibiting LSPRs were ∼5 nm in diameter;[7] moreover, by tracking IR absorbance and elemental composition throughout NC growth, the authors of that study demonstrated that Al was initially excluded and that resulting NCs contained undoped cores ∼2.7 nm in diameter. Our IR spectra of NCs of varied size suggest strongly that AZO NCs synthesized in the nonthermal plasma do not contain similar undoped cores. If they did, then as we decreased AZO NC radius from 11.3 to 3.6 nm, we would expect the volume fraction inaccessible to dopants to increase from ∼9% to ∼65% (assuming a 2.7 nm undoped core and that Al atoms on the surface are mostly electronically inactive, as discussed earlier), resulting in a drastic reduction in the spatially averaged doping level. However, we observe no such trend, which suggests that plasma-synthesized AZO NCs are doped uniformly: the local doping level not only is high beneath the outermost surface layers as discussed earlier but also remains high deep within the cores, near the NC centers.

To explain the absence of undoped cores and the successful doping of small NCs, we propose a simple kinetic model of NC doping in the low-pressure nonthermal plasma. The proposed model is closely related to that proposed by Norris et al.,[15,16] who argued that kinetics, rather than equilibrium thermodynamics, must be used to understand the mechanism of NC doping during colloidal synthesis. This argument is based on the observation that impurity diffusion rates within an NC are very low at typical growth temperatures, and consequently chemical equilibrium between the solid NC and surrounding liquid nutrient cannot be established. The same should be true in the nonthermal plasma provided that plasma power is low enough to maintain sufficiently low NC temperatures.[32] To test this hypothesis, we annealed a film of AZO NCs ($\varphi_{Al} = 1.3\%$) under an Ar atmosphere at 625 °C for 1 h so that the diffusion length of Al in the ZnO lattice[33] was long compared to the NC radius. After annealing, the LSPR is red-shifted to approximately the value typically observed for $\varphi_{Al} = 0$ (Figure S3 in the Supporting Information), indicating that the Al dopants are metastable and that the doped NCs are in fact the product of a nonequilibrium synthesis. Although the term "nonequilibrium plasma" typically refers to the lack of thermal equilibrium among electrons, ions, and neutral species, evidently, here it also describes the synthesis chemistry.

We consider, however, an important difference between colloidal synthesis and plasma synthesis in order to explain radial distributions of dopants in NCs: the former does not occur as far from chemical equilibrium as the latter. The nutrient species in colloidal synthesis are sufficiently stable in solution that the atomistic events leading to nucleation and growth are frequently reversed (dopant and host atoms may return to solution), so that there is a two-way exchange of atoms between the solution and the NC surfaces. Consequently, chemical potential differences between dopant and host atoms incorporated in NCs can significantly influence incorporation rates. Gamelin et al. have demonstrated that because dopants incorporated in the NCs have higher chemical potential than the host atoms (e.g., due to lattice strain[34]), host-atom incorporation can be heavily favored over dopant incorporation, particularly during nucleation and the early stages of growth, resulting in low local doping levels near the centers of solution-synthesized NCs.[35−37] In contrast, the active growth species in plasma synthesis are highly reactive gas-phase ions and radicals with such high chemical potentials that, at sufficiently low temperature, atomistic events leading to nucleation and growth are essentially irreversible (hence ∼12 nm NCs can form in ∼50 ms), and chemical potential differences between incorporated dopant and host atoms are irrelevant (Figure 3a). Additionally, the irreversible NC growth in the plasma is facilitated by the distinctively high reactivities of ligand-free NC surfaces composed of under-coordinated atoms. The schematic in Figure 3b compares doping kinetics in the plasma and in solution: in the plasma, dopants are irreversibly incorporated throughout nucleation and growth.

DOI: 10.1021/acs.nanolett.5b03600
Nano Lett. 2015, 15, 8162−8169

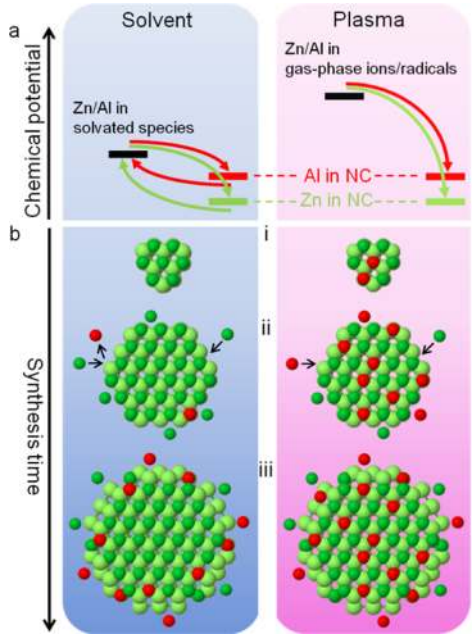

Figure 3. Schematic representations of AZO NC doping in a solvent and in the plasma. Zn, O, and Al atoms are dark green, light green, and red, respectively. (a) A key difference between these environments is that the solvated nutrient species in colloidal synthesis have much lower chemical potential than the gas-phase radicals and ions in plasma synthesis. Consequently, only in solution are atomistic events leading to nucleation and growth frequently reversed, and the higher chemical potential of dopants in NCs (dopants induce more lattice strain than host atoms) can translate to dopant exclusion. (b.i) During nucleation: in solution, doped nuclei, which are relatively unstable, succumb to solvation forces (i.e., critical nucleus size is larger for nuclei containing dopants); in the plasma, doped nuclei persist regardless of strain. (b.ii) During early growth: in solution, dopant incorporation is outcompeted by host-material incorporation; in the plasma, dopants are incorporated essentially whenever they collide with growing NCs. (b.iii) During late growth: in solution, substantial dopant incorporation finally occurs when competing host atoms are sufficiently depleted; in the plasma, dopant incorporation continues as in early growth.

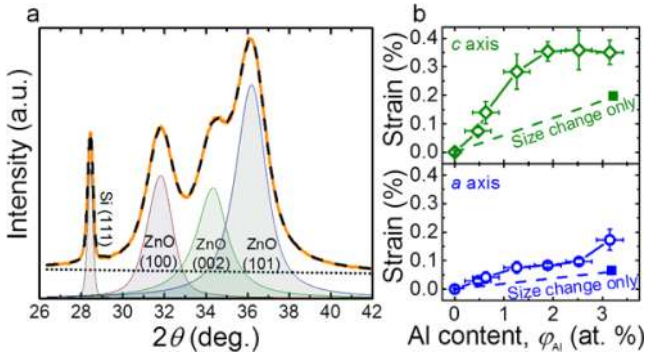

Figure 4. (a) Representative XRD pattern (solid orange line, φ_{Al} = 0.6%) and overall fit (dashed black line) used to determine hexagonal lattice parameters *a* and *c*. The dotted black line is the linear background fit. Each AZO NC sample is mixed with microcrystalline Si powder to obtain a reference peak in the pattern, which is used to eliminate diffractometer alignment errors. (b) Lattice parameters *a* (blue circles) and *c* (green diamonds) extracted from fits of the ZnO (100), (002), (101), and (110) peaks plotted against φ_{Al}. To deconvolute the effects of doping and decreasing NC size (diameter shrinks from 9.5 to ~7 nm as φ_{Al} is increased from 0 to 3.2%), we also determined *a* and *c* of ZnO NCs with diameter similar to that of the smallest AZO NCs (6.6 nm) and found *a* and *c* strains to be merely ~0.06% and ~0.20%, respectively (represented by the solid squares). Thus, we conclude that Al doping introduces a lattice-expanding defect.

The resulting dopant distributions are radially uniform, so that doping level is high even if growth is truncated early.

Our model of nonequilibrium plasma NC synthesis is supported also by the presence of a defect in the plasma-synthesized AZO NCs that is not observed in solution-synthesized AZO NCs. Extracting lattice parameters from XRD patterns of NCs with φ_{Al} ranging from 0 to 3.2%, we find that Al incorporation results in lattice expansion (Figure 4 and Supporting Information Figure S4). In contrast, a similar study of solution-synthesized AZO NCs by Buonsanti et al. revealed lattice *contraction*. They attributed the contraction to the increasing population of substitutional Al: the ionic radii of Al and Zn are 0.53 and 0.74 Å, respectively.[7] This qualitative discrepancy indicates that our NCs contain a lattice-expanding defect much less prevalent in the solution-synthesized NCs, if not completely absent. We tentatively identify the defect as $Al_2^{3+}O_i^{2-}$, that is, two adjacent substitutional Al cations complexed with an interstitial O anion, because its diamagnetism is consistent with the electron paramagnetic resonance (EPR) spectra (Figure S5 in the Supporting Information). This structure has been proposed to explain lattice expansion in AZO films synthesized by RF magnetron sputtering,[38] and its analog has been hypothesized to occur in sputtered Ga-doped ZnO.[39] The precise identity of this lattice-expanding defect, however, is not essential to our argument; in any case, its abundance in our NCs serves as additional evidence of fundamentally different impurity incorporation kinetics.

Although the unique synthesis kinetics in the nonequilibrium plasma result in high local doping levels near the NC centers, a substantial portion of Al atoms do reside on NC surfaces, as indicated by STEM-EELS elemental maps. Electrical resistivity measurements and chemical etching experiments reveal that these Al atoms are oxidized. Following procedures described in ref 16 (wherein only vacancy-doped ZnO was studied), we deposited films with φ_{Al} ranging from 0 to 3.2% on glass substrates, coated them with Al_2O_3 using ALD, and then deposited Al electrodes by thermal evaporation for four-point-probe current–voltage measurements. For φ_{Al} = 0, the resistivity is ~2 Ω cm, similar to that reported in ref 16, and much lower (more than 8 orders of magnitude) than that typically measured in a film composed of NCs covered in insulating ligands.[40] However, as shown in Figure 5, resistivity increases by nearly an order of magnitude as φ_{Al} is increased to 3.2%. We hypothesized that this counterintuitive rise in resistivity upon increasing φ_{Al} is due to higher charge-transport resistance across NC-NC interfaces, and we attributed this increased resistance to oxidized surface-bound Al and Al_2O_3 clusters (see Figure 1c) formed on the NC surfaces during synthesis. (The Al_2O_3 grown on the NC surfaces using ALD *after* film deposition removes traps and reduces resistance, whereas the Al_2O_3 formed *during* NC synthesis and pinched between adjacent NCs increases resistance.) To test this hypothesis, we introduced a selective chemical etching step between NC deposition and ALD coating: we soaked the films in a sodium carbonate/bicarbonate solution at pH 10 where ZnO is stable but Al_2O_3 dissolves. In an etched NC film (φ_{Al} = 1.9%), NC size (from XRD) was not reduced, but Al content

DOI: 10.1021/acs.nanolett.5b03600
Nano Lett. 2015, 15, 8162–8169

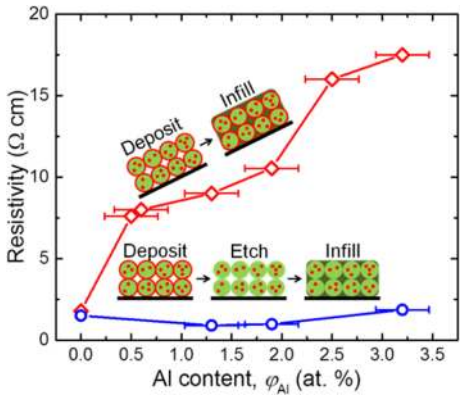

Figure 5. Electrical resistivity of films comprising AZO NCs vs φ_{Al} with and without selective chemical etching to remove Al_2O_3 on NC surfaces. The increase in resistivity of films produced without an etching step (red diamonds) is attributed to Al_2O_3 formed during synthesis which can reside at particle−particle interfaces, forming insulating barriers which impede charge transport (unlike the Al_2O_3 from ALD which cannot form between intimately connected particles). Resistivities of films produced with an etching step (blue circles) are significantly lower than those of films that are not etched, but an improvement with doping is still lacking. This could be due to incomplete removal of Al_2O_3 or to a canceling effect of the NC size reduction (9.5 to ∼7 nm) accompanying doping (e.g., more grain boundary scattering).

(from energy dispersive X-ray spectroscopy) was reduced by ∼40%, indicating that oxidized Al does reside on NC surfaces and is selectively removed by etching. Furthermore, in all etched films, resistivity is significantly lower (by a factor of 3 to 7) compared with that of unetched films, confirming our hypothesis. Indeed, even after etching, the highest resistance to charge transport in these films is still at the NC-NC boundaries. Using n_e and μ_e values extracted from IR measurements (Figure 1f), we estimate that the intraparticle resistivity is $\sim 7 \times 10^{-3}$ Ω cm for $\varphi_{Al} = 0$ and $\sim 3 \times 10^{-3}$ Ω cm for $\varphi_{Al} = 3.2\%$, significantly lower than the film resistivities measured electrically (1−2 Ω cm). Thus, the initially counterintuitive rise in resistivity upon increasing φ_{Al} is not surprising: enhancement of the dominant resistance source (interparticle resistance) by Al_2O_3 pinched between NCs outweighs the resistance reduction due to doping.

Oxidation of dopant atoms prior to incorporation in NCs is an inherent competitive reaction path which must be addressed in further development of plasma synthesis of doped metal oxide NCs. The kinetic processes that enable the survival of doped nuclei also permit the persistence of small clusters of oxidized dopants. One approach to explore is downstream injection of additional dopant precursor to replenish the supply of unoxidized dopant atoms.

In conclusion, we have demonstrated that nonthermal plasma synthesis is a promising route toward addressing several challenges in doping metal oxide NCs. The key advantage of the plasma synthesis approach is the unique NC nucleation and growth kinetics that arise from irreversible interactions among highly reactive gas-phase ions and radicals and ligand-free NC surfaces. Exploiting these thoroughly nonequilibrium conditions, we have synthesized uniformly doped AZO NCs with high dopant activation fractions and high local doping levels in their central cores. Hence, we have been able to maintain high doping levels while reducing NC size, experimentally demonstrating for the first time a quantum confinement effect on the LSPR energy in vacancy- and impurity-doped semiconductor NCs. We have also detected electronically inactive defects and surface-bound oxidized dopants, revealing challenges presented by plasma synthesis kinetics that should be considered as this synthesis approach is expanded to produce other doped metal oxide NCs and nanocrystalline thin films.

Methods. *AZO NC Synthesis and Deposition.* A detailed description of ZnO NC synthesis and deposition accompanied by a schematic of the synthesis/deposition system is provided in ref 16; to synthesize AZO NCs, TMA is injected into the same reactor port as DEZ. Briefly, in a typical synthesis, the DEZ and TMA are injected into an Ar/O_2 plasma (270 SCCM of Ar, 30 SCCM of O_2) in a cylindrical pyrex reaction chamber with a ∼30 cm length and 0.75 in. inner diameter. The DEZ and TMA are delivered as vapors via bubblers using Ar as the carrier gas. To control the DEZ and TMA feed rates, the carrier gas feed rates are held constant (20 SCCM through the DEZ bubbler and 3 SCCM through the TMA bubbler), and the bubbler pressures are controlled with metering valves: the DEZ bubbler pressure is held at 80 Torr while the TMA bubbler pressure is varied from 800 to 120 Torr to produce NCs with φ_{Al} ranging from 0.5 to 3.2%. The aerosol containing AZO NCs formed in the reaction chamber is accelerated through a rectangular slit orifice into a second chamber evacuated to 1.4×10^{-3} Torr using a Leybold Turbovac 1000c turbo pump. In this lower-pressure chamber, the NCs form a particle beam with thin rectangular cross section defined by the slit and deposit via inertial impaction onto various substrates (glass, Si, and NaCl) mounted to a pushrod, which linearly oscillates at a frequency of 1 Hz perpendicularly to the particle beam to produce rectangular thin films. A deposition time of 30 s produces films approximately 500 nm in thickness. To vary NC size, four different slit orifices are used: all are 15 mm long with widths ranging from 0.5 to 3.5 mm so that the pressure in the reaction chamber ranges from 14.5 to 0.9 Torr. The plasma is generated by applying a radio frequency (13.56 MHz) voltage to a pair of copper ring electrodes encircling the Ar/O_2 injection port. A custom impedance matching network is used to attain a forward power of 100 W and a reflected power ≤2 W.

Atomic Layer Deposition. For FTIR, UV−vis, and electrical resistivity measurements, AZO NCs are coated in Al_2O_3 using a Cambridge Nanotech/Ultratech Savannah S200 ALD reactor. The ALD process is carried out at 180 °C and 0.5 Torr. One deposition cycle consists of four steps: (1) a 0.1 s H_2O pulse, (2) a 30 s nitrogen purge, (3) a 0.1 s TMA pulse, and (4) a 30 s nitrogen purge; 70 cycles are completed for a 7.7 nm coating. Prior to these cycles, the AZO NCs are allowed to outgas for 2000 s under 20-SCCM nitrogen flow.

Spectroscopy. Film thicknesses and porosities are determined by spectroscopic ellipsometry: AZO NCs are deposited onto Si wafers and measured using a J.A. Woolam M44 spectrometer, and spectra between 450 and 750 nm are fitted using the Bruggeman effective medium approximation. Unless otherwise stated, films characterized in this work are 500 ± 50 nm thick with 65 ± 5% porosity (ZnO volume fractions of ∼35%). For FTIR spectroscopy, AZO NCs are deposited onto IR-transparent polished NaCl plates and coated with 7.7 nm of Al_2O_3 by ALD, and measurements are performed using a Bruker Alpha IR spectrometer in transmission mode. The AZO NC films are exposed to air both before and after ALD, but measurements are performed under a nitrogen atmosphere. For large NCs (diameter ≥7 nm), LSPR absorption features are

DOI: 10.1021/acs.nanolett.5b03600
Nano Lett. 2015, 15, 8162−8169

fitted using Mie theory with the classical Drude dielectric function, assuming frequency-independent damping (for details, see ref 16). For UV−vis spectroscopy, AZO NCs are deposited onto Corning Eagle XG glass substrates and coated with 7.7 nm of Al_2O_3 by ALD (unless stated otherwise) and then measured in air using an Agilent Cary 5000 spectrophotometer in transmission mode. Bandgaps are determined from Tauc plots for a direct bandgap semiconductor ($(\alpha h\nu)^2$ vs $h\nu$). For EPR spectroscopy, thick (~3 μm) AZO NC films are deposited onto Si wafers and then scraped into Suprasil quartz tubes. Measurements are performed in air using a Bruker Continuous Wave Elexsys E500 EPR spectrometer. For inductively coupled plasma mass spectroscopy, thick (~3 μm) AZO NC films are deposited onto Si wafers and then digested in nitric acid. A yttrium internal standard is added (40 ppb), and then the solution is analyzed using a Thermo Scientific XSERIES 2 ICP-MS equipped with an ESI PC3 Peltier-cooled spray chamber, SC-FAST injection loop, and SC-4 autosampler. All measurements are performed in standard mode (no collision gas).

X-ray Diffraction. XRD measurements are performed using a Bruker D8 Discover diffractometer equipped with a beryllium area detector (angular resolution = 0.02°) and a cobalt-Kα source; the collected patterns are mathematically converted to copper-Kα patterns. For typical XRD measurements used to determine NC size, AZO NCs are directly deposited by inertial impaction onto Si wafers and not coated by ALD. Average NC sizes are calculated using the Scherrer equation, assuming spherical particles.[41] For more precise XRD measurements used to determine lattice parameters, a mixture of AZO NCs and microcrystalline Si powder (~10% Si by mass) is sonicated in ethanol and then dropcast onto Si wafers; the resulting Si (111) peak in the diffraction pattern is used as a reference to correct for alignment discrepancies. Lattice parameters are determined as follows. First, each sample is measured three times with the X-ray beam probing a different portion of the sample each time to minimize the influence of any spatial inhomogeneities in the AZO/Si mixture. Then XRD patterns are fitted with pseudo-Voigt profiles using MDI Jade. The best fits are achieved by splitting each pattern in two and using a linear background for the low-angle half (<42°) and a parabolic background for the high-angle half. The fits are linearly shifted so that all Si (111) peaks align. Using these aligned fits, the hexagonal lattice parameter a is extracted from the locations of the ZnO (100) and (110) peaks, and then this a value is used in conjunction with the locations of the ZnO (002) and (101) peaks to determine the lattice parameter c. The ZnO (102) peak is neglected due to its strong overlap with the Si (220) peak. For each sample, the reported a and c values are averages of the triplicate measurements, and the error bars represent the standard deviations. For lattice spacings up to 3.2 Å, the beryllium area detector's angular resolution (0.02°) translates to uncertainties up to ±0.0009 Å, or ±0.03% in strain units. Error bars exceeding this magnitude are likely due to residual random alignment errors.

Transmission Electron Microscopy and Spatially Resolved Electron Energy Loss Spectroscopy. AZO NCs are deposited by inertial impaction directly onto carbon-coated gold TEM grids (ultrathin carbon/holey support). STEM-EELS data are acquired on an aberration-corrected FEI Titan G2 60−300 (S)TEM equipped with a Gatan Enfinium ER EEL spectrometer, operating at 60 keV, 30 mrad convergence angle, 75 pA beam current, and a 25.9 mrad EELS aperture. Spectrum images are acquired by scanning the beam across clusters of NCs with ~7 Å steps with a 60 ms pixel dwell time in a 60 × 60 pixel grid while simultaneously collecting HAADF signal and EEL spectra at 15−527 eV (Al L-edge), and 700−1212 eV (Zn L-edge) with an energy dispersion of 0.25 eV. To mitigate damage to the specimen, 64 × 64 subpixel scanning is implemented to evenly distribute the dose over the NCs. Background signals are subtracted using a power-law fitting function. The Al $L_{2,3}$ (72−88 eV, avoiding the Zn M edge at 88 eV) and Zn $L_{2,3}$ (1020−1212 eV) edges at each pixel are integrated for each pixel and a 3-pixel Gaussian blur is applied to the final spectrum images to reduce noise. For verification of NC sizes, lower-resolution micrographs are obtained using an FEI Tecnai T12 TEM.

Electrical Resistivity Measurements and Selective Etching of Oxidized Al. AZO NCs are deposited onto 1 × 1 cm Corning Eagle XG glass substrates and coated with 7.7 nm of Al_2O_3 by ALD. For four-point measurements, four parallel 500 nm thick Al line electrodes are deposited onto the film by thermal evaporation with a spacing of 2 mm between adjacent lines. Using a Janis Research Cryomicroprobe Station connected to an Agilent 4155C semiconductor parameter analyzer, current is controlled between the outer electrodes and voltage is measured between the inner electrodes. These measurements are performed in air at room temperature. To remove oxidized Al residing on NC surfaces, chemical etching is performed between NC deposition and ALD coating. Films are soaked in a sodium carbonate/bicarbonate solution at pH 10 for 1 h and then dried in air at 100 °C.

■ ASSOCIATED CONTENT

Supporting Information

The Supporting Information is available free of charge on the ACS Publications website at DOI: 10.1021/acs.nanolett.5b03600.

Al concentrations from ICP-MS; XRD patterns, TEM images, and UV−vis spectra of NCs with varied size; FTIR spectra before and after thermal annealing; XRD patterns and UV−vis and EPR spectra of NCs with varied φ_{Al}. (PDF)

■ AUTHOR INFORMATION

Corresponding Author

*E-mail: kortshagen@umn.edu.

Author Contributions

B.L.G. synthesized NCs and performed XRD, FTIR, and UV−vis measurements. S.G. synthesized NCs and performed FTIR, low-resolution TEM, and electrical resistivity measurements. J.T.H. performed STEM-EELS measurements and elemental mapping. N.J.K. performed EPR measurements. K.A.M., E.S.A., and U.R.K. supervised the project and contributed to data interpretation. All authors participated in discussions of results and preparation of the manuscript.

Notes

The authors declare no competing financial interest.

■ ACKNOWLEDGMENTS

This work was supported primarily by the National Science Foundation through the University of Minnesota MRSEC under Award Number DMR-1420013 and partially by BASF Corporation. Parts of this work were carried out in the College of Science and Engineering Characterization Facility, University

DOI: 10.1021/acs.nanolett.5b03600
Nano Lett. 2015, 15, 8162−8169

of Minnesota, which has received capital equipment funding from the NSF through the UMN MRSEC program under Award Number DMR-1420013. Parts of this work were carried out in the College of Science and Engineering Minnesota Nanocenter, University of Minnesota, which receives partial support from the NSF through the NNIN program. We thank Rick Knurr for ICP-MS measurements. We thank Dr. Javier Garcia Barriocanal, Professor Alexander Govorov, Professor Michael Manno, and Professor Elijah Thimsen for valuable discussions.

REFERENCES

(1) Manthiram, K.; Alivisatos, A. P. *J. Am. Chem. Soc.* **2012**, *134*, 3995−3998.
(2) Wang, T.; Radovanovic, P. V. *J. Phys. Chem. C* **2011**, *115*, 406−413.
(3) Lounis, S. D.; Runnerstrom, E. L.; Bergerud, A.; Nordlund, D.; Milliron, D. J. *J. Am. Chem. Soc.* **2014**, *136*, 7110−7116.
(4) Kanehara, M.; Koike, H.; Yoshinaga, T.; Teranishi, T. *J. Am. Chem. Soc.* **2009**, *131*, 17736−17737.
(5) Gordon, T. R.; Paik, T.; Klein, D. R.; Naik, G. V.; Caglayan, H.; Boltasseva, A.; Murray, C. B. *Nano Lett.* **2013**, *13*, 2857−2863.
(6) De Trizio, L.; Buonsanti, R.; Schimpf, A. M.; Llordes, A.; Gamelin, D. R.; Simonutti, R.; Milliron, D. J. *Chem. Mater.* **2013**, *25*, 3383−3390.
(7) Buonsanti, R.; Llordes, A.; Aloni, S.; Helms, B. A.; Milliron, D. J. *Nano Lett.* **2011**, *11*, 4706−4710.
(8) Schimpf, A. M.; Ochsenbein, S. T.; Buonsanti, R.; Milliron, D. J.; Gamelin, D. R. *Chem. Commun.* **2012**, *48*, 9352−9354.
(9) Gaspera, E. D.; Bersani, M.; Cittadini, M.; Guglielmi, M.; Pagani, D.; Noriega, R.; Mehra, S.; Salleo, A.; Martucci, A. *J. Am. Chem. Soc.* **2013**, *135*, 3439−3448.
(10) Runnerstrom, E. L.; Llordes, A.; Lounis, S. D.; Milliron, D. J. *Chem. Commun.* **2014**, *50*, 10555−10572.
(11) Clavero, C. *Nat. Photonics* **2014**, *8*, 95−103.
(12) Das, N. C. *J. Appl. Phys.* **2011**, *110*, 046101.
(13) Kundu, J.; Le, F.; Nordlander, P.; Halas, N. J. *Chem. Phys. Lett.* **2008**, *452*, 115−119.
(14) Schimpf, A. M.; Thakkar, N.; Gunthardt, C. E.; Masiello, D. J.; Gamelin, D. R. *ACS Nano* **2014**, *8*, 1065−1072.
(15) Norris, D. J.; Efros, A. L.; Erwin, S. C. *Science* **2008**, *319*, 1776−1779.
(16) Erwin, S. C.; Zu, L.; Haftel, M. I.; Efros, A. L.; Kennedy, T. A.; Norris, D. J. *Nature* **2005**, *436*, 91−94.
(17) Buonsanti, R.; Milliron, D. J. *Chem. Mater.* **2013**, *25*, 1305−1317.
(18) Vlaskin, V. A.; Barrows, C. J.; Erickson, C. S.; Gamelin, D. R. *J. Am. Chem. Soc.* **2013**, *135*, 14380−14389.
(19) Rowe, D. J.; Jeong, J. S.; Mkhoyan, K. A.; Kortshagen, U. R. *Nano Lett.* **2013**, *13*, 1317−1322.
(20) Holman, Z. C.; Kortshagen, U. R. *Nanotechnology* **2010**, *21*, 335302.
(21) Thimsen, E.; Johnson, M.; Zhang, X.; Wagner, A. J.; Mkhoyan, K. A.; Kortshagen, U. R.; Aydil, E. S. *Nat. Commun.* **2014**, *5*, 5822.
(22) Vollmer, M.; Kreibig, U. *Optical properties of metal clusters*; Series on Material Science; Springer: New York, 1995.
(23) Lu, J. G.; Fujita, S.; Kawaharamura, T.; Nishinaka, H.; Kamada, Y.; Ohshima, T.; Ye, Z. Z.; Zeng, Y. J.; Zhang, Y. Z.; Zhu, L. P.; He, H. P.; Zhao, B. H. *J. Appl. Phys.* **2007**, *101*, 083705.
(24) Mendelsberg, R. J.; Garcia, G.; Li, H.; Manna, L.; Milliron, D. J. *J. Phys. Chem. C* **2012**, *116*, 12226−12231.
(25) Ghosh, S. K.; Pal, T. *Chem. Rev.* **2007**, *107*, 4797−4862.
(26) Halperin, W. P. *Rev. Mod. Phys.* **1986**, *58*, 533−606.
(27) Kreibig, U.; Genzel, L. *Surf. Sci.* **1985**, *156*, 678−700.
(28) Halas, N. J.; Lal, S.; Chang, W.; Link, S.; Nordlander, P. *Chem. Rev.* **2011**, *111*, 3913−3961.
(29) Tame, M. S.; McEnery, K. R.; Özdemir, Ş. K.; Lee, J.; Maier, S. A.; Kim, M. S. *Nat. Phys.* **2013**, *9*, 329−340.
(30) Scholl, J. A.; Koh, A. L.; Dionne, J. A. *Nature* **2012**, *483*, 421−427.
(31) Zhang, H.; Kulkarni, V.; Prodan, E.; Nordlander, P.; Govorov, A. O. *J. Phys. Chem. C* **2014**, *118*, 16035−16042.
(32) Kramer, N. J.; Anthony, R. J.; Mamunuru, M.; Aydil, E. S.; Kortshagen, U. R. *J. Phys. D: Appl. Phys.* **2014**, *47*, 075202.
(33) Norman, V. J. *Aust. J. Chem.* **1969**, *22*, 325−329.
(34) Vegard, L. *Eur. Phys. J. A* **1921**, *5*, 17−26.
(35) Bryan, J. D.; Gamelin, D. R. *Prog. Inorg. Chem.* **2005**, *54*, 47−126.
(36) Beaulac, R.; Archer, P. I.; Ochsenbein, S. T.; Gamelin, D. R. *Adv. Funct. Mater.* **2008**, *18*, 3873−3891.
(37) Schwartz, D. A.; Norberg, N. S.; Nguyen, Q. P.; Parker, J. M.; Gamelin, D. R. *J. Am. Chem. Soc.* **2003**, *125*, 13205−13218.
(38) Yung-I, C.; Jenq-Gong, D. *Mater. Chem. Phys.* **1991**, *27*, 427−439.
(39) Roberts, N.; Wang, R. P.; Sleight, A. W.; Warren, W. W. *Phys. Rev. B: Condens. Matter Mater. Phys.* **1998**, *57*, 5734−5741.
(40) Kovalenko, M. V.; Scheele, M.; Talapin, D. V. *Science* **2009**, *324*, 1417−1420.
(41) Borchert, H.; Shevchenko, E. V.; Robert, A.; Mekis, I.; Kornowski, A.; Grübel, G.; Weller, H. *Langmuir* **2005**, *21*, 1931−1936.

DOI: 10.1021/acs.nanolett.5b03600
Nano Lett. 2015, 15, 8162−8169